

PAPER • OPEN ACCESS

Enhanced magnetic transduction of neuronal activity by nanofabricated inductors quantified via finite element analysis

To cite this article: Jack Phillips *et al* 2022 *J. Neural Eng.* **19** 046003

View the [article online](#) for updates and enhancements.

You may also like

- [Equilibrium and non-equilibrium microfireball behaviour in light-ion fusion systems](#)
M. Uesaka, R.R. Peterson and G.A. Moses
- [A methodology for evaluating the effects of climate change on climatic design conditions for buildings and application to a case study in Madison, Wisconsin](#)
. Gesangyangji, Daniel Vimont, Tracey Holloway et al.
- [Observations of Dynamic Behaviour of a Linear Turbulently-Heated Plasma Using Microwave Scattering](#)
Osamu Asada, Kazuo Yoshioka, Akira Inoue et al.



PAPER

OPEN ACCESS

RECEIVED

31 December 2021

REVISED

24 May 2022

ACCEPTED FOR PUBLICATION

15 June 2022

PUBLISHED

1 July 2022

Original content from this work may be used under the terms of the [Creative Commons Attribution 4.0 licence](https://creativecommons.org/licenses/by/4.0/).

Any further distribution of this work must maintain attribution to the author(s) and the title of the work, journal citation and DOI.



Enhanced magnetic transduction of neuronal activity by nanofabricated inductors quantified via finite element analysis

Jack Phillips^{1,3} , Mitchell Glodowski¹, Yash Gokhale¹, Matthew Dwyer^{1,2}, Alireza Ashtiani¹  and Aviad Hai^{1,2,3,*} 

¹ Department of Biomedical Engineering, University of Wisconsin–Madison, Madison, WI, 53706, United States of America

² Department of Electrical and Computer Engineering, University of Wisconsin–Madison, Madison, WI, 53706, United States of America

³ Wisconsin Institute for Translational Neuroengineering (WITNe), University of Wisconsin–Madison, Madison, WI, 53706, United States of America

* Author to whom any correspondence should be addressed.

E-mail: ahai@wisc.edu

Keywords: magnetic fields, signals, device, methods, single neuron, recording, transduction

Supplementary material for this article is available [online](#)

Abstract

Objective. Methods for the detection of neural signals involve a compromise between invasiveness, spatiotemporal resolution, and the number of neurons or brain regions recorded. Electrode-based probes provide excellent response but usually require transcranial wiring and capture activity from limited neuronal populations. Noninvasive methods such as electroencephalography and magnetoencephalography offer fast readouts of field potentials or biomagnetic signals, respectively, but have spatial constraints that prohibit recording from single neurons. A cell-sized device that enhances neurogenic magnetic fields can be used as an *in situ* sensor for magnetic-based modalities and increase the ability to detect diverse signals across multiple brain regions. **Approach.** We designed and modeled a device capable of forming a tight electromagnetic junction with single neurons, thereby transducing changes in cellular potential to magnetic field perturbations by driving current through a nanofabricated inductor element. **Main results.** We present detailed quantification of the device performance using realistic finite element simulations with signals and geometries acquired from patch-clamped neurons *in vitro* and demonstrate the capability of the device to produce magnetic signals readable via existing modalities. We compare the magnetic output of the device to intrinsic neuronal magnetic fields (NMFs) and show that the transduced magnetic field intensity from a single neuron is more than three-fold higher at its peak (1.62 nT vs 0.51 nT). Importantly, we report on a large spatial enhancement of the transduced magnetic field output within a typical voxel ($40 \times 40 \times 10 \mu\text{m}$) over 250 times higher than the intrinsic NMF strength (0.64 nT vs 2.5 pT). We use this framework to perform optimizations of device performance based on nanofabrication constraints and material choices. **Significance.** Our quantifications institute a foundation for synthesizing and applying electromagnetic sensors for detecting brain activity and can serve as a general method for quantifying recording devices at the single cell level.

1. Introduction

From basic neuroscience to neurology, the ability to decode neural activity with minimized invasiveness and little compromise to spatiotemporal precision has long been the goal of experimenters and clinicians [1–3]. Implantable electrodes are the most typical brain interface allowing for single-neuron electrophysiological readouts, but they are invasive,

requiring long-term transcranial connections with readouts limited by the size of the device [4, 5]. Techniques such as electroencephalography (EEG) and magnetoencephalography (MEG) offer an entirely noninvasive alternative, enabling remote recording of electrophysiological signals at the scalp, but do not provide readouts at single-neuron resolution [6, 7]. Due to amplitude attenuation and spatial distortion of local field potentials (LFPs) through neural tissue

and the skull, EEG provides a measure of LFPs originating from large aggregates of neurons within the cortex, with spatially shifted readouts and signal amplitude attenuation proportional to the square of the distance from its source [6, 8]. In contrast, magnetic fields in the brain are only minutely attenuated or distorted, and can therefore be detected with higher spatial precision and improved localization using sensitive magnetometers [7, 9]. MEG readouts still arise from large populations of neurons firing synchronously, and likely reflect activity developing from neural currents within shallow areas of cortical sulci that are properly aligned to the magnetic detection devices [7]. Bridging the gap between noninvasive neuroimaging and single-neuron invasive electrophysiology can potentially open the door to a new milieu of brain readouts.

Quantifications of intrinsic neuronal magnetic fields (NMFs) arising from the excitation of single neurons, subcellular compartments, and multicellular neuronal populations, were carried out computationally by several groups and can determine possibilities for NMF detection without the need for invasive transcranial wiring at the time of recording [10–13]. These studies informed the interpretation of MEG recordings [7, 14] and catalyzed the design of specialized pulse sequences, phantom measurements and distilled preparations for magnetic resonance imaging (MRI) in attempts to detect NMFs volumetrically [15–19]. To date, real-time detection of NMFs by MEG at native *in vivo* scenarios, in the presence of motion artifacts, and blood flow related electromagnetic disturbances [7, 20, 21] requires severe averaging of consecutive trials evoking coordinated activity of many neurons, and has not yet been demonstrated convincingly by volumetric modalities [15, 22]. This points to a requirement for *in situ* agents similar to emerging contrast agents for direct neuroimaging of calcium [23–25] and neurotransmitters [26–29], that could similarly facilitate direct detection of NMFs across the brain.

Here, we present an approach for enhancing magnetic fields in response to intrinsic electrophysiological events using nanofabricated planar inductors that are interfaced with single neurons and designed to act as agents that transduce neural activity into readable magnetic signals. The interface relies on high electromagnetic coupling promoted by nanofabricated protrusions previously shown to generate a tight cleft between cells and electrodes [30, 31] and to yield increased electrical response to neural activity [32–34]. Using a realistic finite element framework with nanometer scale resolution, we quantify the ionic fluctuations induced in the neuron coupled to the device by using patch clamp recordings of mammalian cortical neurons as signal input. We quantify the voltage drop developing between the interface pad at the center of the inductor and an extended reference pad facing the extracellular solution, and

then determine the amplitude and spatiotemporal characteristics of the magnetic field response resulting from membrane potential changes that drive current through the device. We use our results to perform optimizations of the geometry of the device while conforming to nanofabrication constraints and reach an optimized design that is able to transduce electrophysiological signals to a magnetic field approximately 300 times greater in magnitude perpendicular to the plane of the inductor and cell culture surface than those produced intrinsically by individual neurons when averaged across a volume. Our approach could immediately enable sensitive detection of single-neuron activity *in vitro* and pave the way for potential future designs applied with modalities such as MEG and MRI.

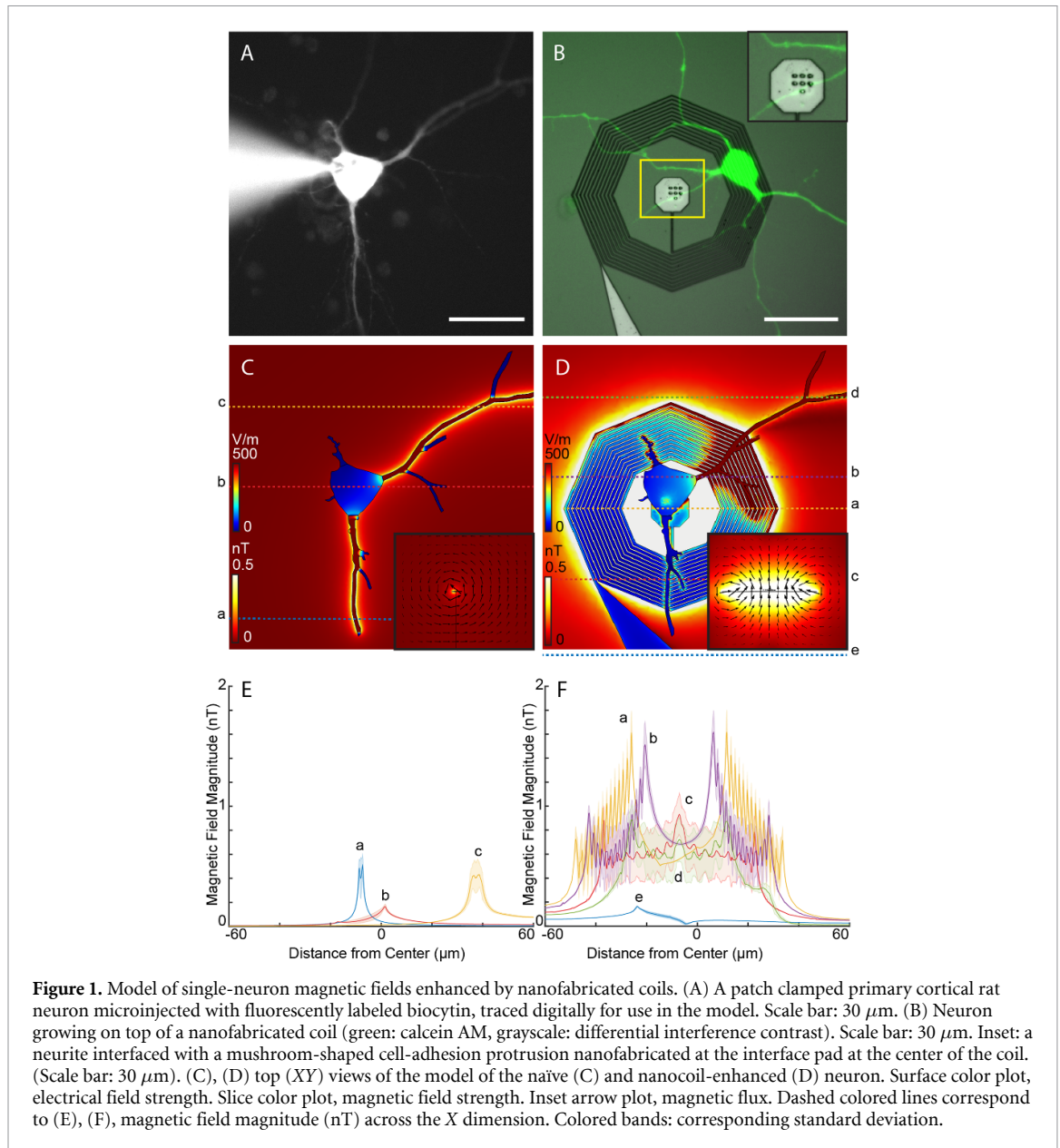
2. Methods

2.1. Device fabrication

Devices were fabricated by electron beam lithography on glass or high resistivity silicon dies. A2/A4/A6 poly methyl-methacrylate (PMMA) 495 (Kayaku Advanced Materials Inc. MA, USA) was spin-coated on samples at 3000 RPM for 30 s and baked in a convection oven for 30 min. Direct write of inductor patterns was then performed by electron beam lithography (Elionix, Tokyo, Japan) followed by development of the resist using methyl isobutyl ketone/isopropyl alcohol (MIBK/IPA) (1:2). Ti/Au (1:10) was deposited by electron beam deposition followed by PMMA lift off in ultrasonicated acetone (5 min) at room temperature. Silicon oxide insulating layer was deposited by plasma-enhanced chemical vapor deposition. An additional nanolithography step was performed to define the ground pad and protruding pillars at the interface pad, followed by buffered oxide etching through the silicon oxide layer. Au protrusions were grown by electron beam deposition PMMA was lift off. Samples were then cleaned in IPA and cultured with neurons as described below to demonstrate biocompatibility (figure 1(b)). The device optimization described below uses a device geometry successfully fabricated in this way as a starting point.

2.2. *In vitro* cell culture

Primary cortical neurons were cultured on substrates following previously described protocols [35]. Glass or device surface was sterilized for 15 min in ethanol, then a portion of each sample was prepared with a 50 μ l droplet of sterile filtered aqueous 0.1 mg ml⁻¹ poly-d-lysine (Gibco A38904-01) and 4 μ g ml⁻¹ laminin (Gibco 23017-015). Coverslips sat for 60 min in incubator conditions (37 °C, 5% CO₂, 95% humidity), were rinsed three times with 1x phosphate buffered saline (PBS), then stored at 4 °C overnight. Primary cortical rat neurons (Gibco A10840-01, Lot 2111507) were thawed from dry ice



(-80°C) for 2 min without agitation in a 37°C water bath. A 15 ml conical tube and 1 ml micropipette tip were rinsed with plating media (Neurobasal Plus, Gibco A3582901; 10% FBS Gibco 10437010; $1\times$ GlutaMAX, Gibco 35050-061), the tip was used to transfer the cell suspension from the cryotube to the conical tube, 1 ml of plating media was added dropwise for a final concentration of $500\,000\text{ cells ml}^{-1}$, and $300\ \mu\text{l}$ of cell suspension ($150\,000\text{ cells}$) were plated onto each sample. The cultures sat in incubator conditions for 4 h before plating media was removed and 3 ml maintenance media (Neurobasal Plus, $1\times$ B27 Plus Gibco A3582801, $1\times$ GlutaMAX) were added to each 35 mm well. 1.5 ml media changes were performed every 3–4 days (Mondays and Fridays). Cells on devices were stained with $10\ \mu\text{g ml}^{-1}$ calcein AM (Invitrogen C3099) in media for 20 min at 37°C followed by a 20 min rest in stain-free media at 37°C before imaging for visualization (figure 1(b)).

2.3. Patch clamp recordings

At 24 days *in vitro* (DIV) samples on glass coverslips were removed from maintenance media and placed in extracellular solution (ECS; in mM, NaCl 145, KCl 5, MgCl_2 1, CaCl_2 1, HEPES 5, Glucose 5, Sucrose 20, D-serine 0.01, adjusted to pH 7.4 with NaOH and 315 mOsm with sucrose). All solutions were prepared with culture grade H_2O (Corning 25-055-CVC). Filamented glass pipettes (8250 Glass, A-M Systems 596800) were pulled on a P-97 pipette puller (Sutter Instruments, Novato, CA) to create 5–10 M Ω micropipettes. Pipettes were backfilled with intracellular solution (ICS; in mM, KCl 120, HEPES 10, ATP.Na 5, GTP.Na 0.2, EGTA 10, adjusted to pH 7.2 with KOH), mounted on a Sutter IPA Headstage with a Ag/AgCl coated wire driven by a Sutter Quad micromanipulator and connected to a Sutter Double IPA patch clamp amplifier for recording via SutterPatch (v. 2.04, Sutter Instruments,

Novato, CA) within Igor Pro software (v. 8.04, WaveMetrics, Portland, OR) in current clamp configuration. For staining experiments, ICS included 20 μM of biocytin (Sigma B4261). Upon breaking through the plasma membrane, biocytin diffused into the cell, allowing imaging of the neuron processes for morphological registration used for simulations (figure 1(a)). Electrophysiology experiments were performed using Olympus BX51WIF microscope (Olympus America Inc., Waltham, MA) and ORCA-Flash4.0 V3 C13440 Digital sCMOS camera (Hamamatsu, Japan) for optical acquisition during biocytin injection.

2.4. Model neuron

Biocytin-injected neuron morphology (figure 1(a)) was traced to create a vector representation, which was imported into COMSOL multiphysics simulation environment (COMSOL Inc., Stockholm, Sweden). Geometry was extruded to a height of 1.1 μm (figure 1(c)). The membrane was modeled with exterior surface area 1450 μm^2 , volume 14.39 μm^3 , relative permeability $\varepsilon = 1$, relative permittivity $\mu = 1$, electrical conductivity $\sigma = 1 \times 10^{-13} \text{ S m}^{-1}$, surrounding the intracellular environment, surface area 1431.1 μm^2 , volume 463.77 μm^3 , which was modeled using the electrical properties of cerebrospinal fluid, $\varepsilon = 1.09 \times 10^2$, $\mu = 1$, $\sigma = 2 \text{ S m}^{-1}$. Representative action potential (AP) data was extracted from voltage traces of current clamp recordings (figure 3(a), sampling frequency = 6103.5 Hz, total recording time 23:51.768) and used as input for an electronic circuit simulation software (LTSPICE, Analog Devices, Norwood, MA). The cell-device interface was simulated as a 100 M Ω resistor in parallel with a 15 pF capacitor. The current was measured across this interface and downsampled to 20 key values, which were applied as inputs in COMSOL on one face of the neuron in a parametric sweep stationary study for simulations of magnetic flux density and field strength during APs to compare the response of the naïve model neuron to that of the modeled cell-device interface (figure 3(c)).

2.5. Device modeling and optimization

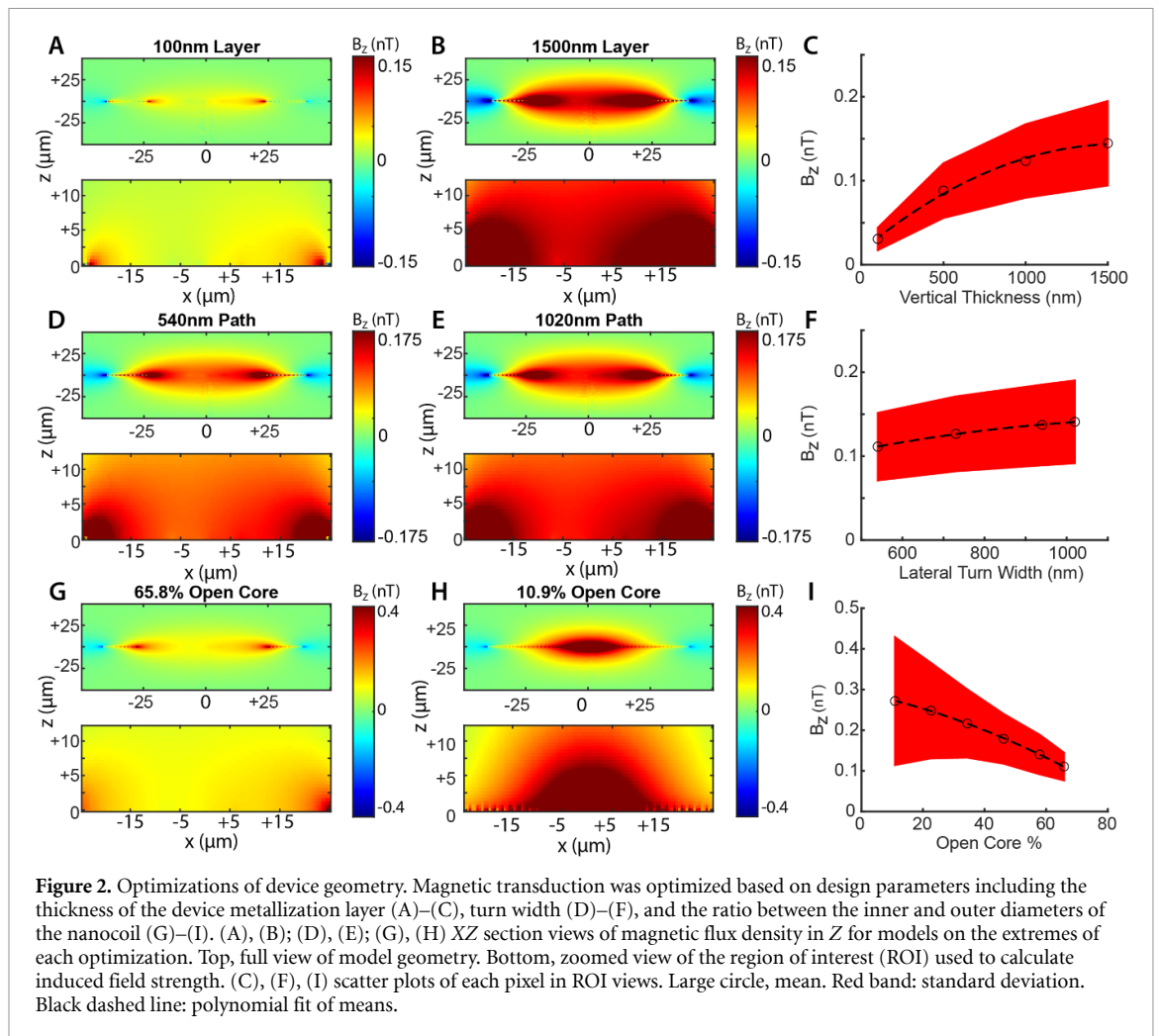
Simulations and optimizations of device response and device-neuron interface were performed in COMSOL. Patterns used for nanofabrication were imported and extruded along the z -axis. The electrical properties of the device were set to those of gold, $\varepsilon = 1$, $\mu = 1$, $\sigma = 1 \times 10^6 \text{ S m}^{-1}$. This gold layer thickness was tested at 100, 500, 1000, and 1500 nm. Lateral width of the inductor conducting turns was tested at 540, 730, 940, and 1020 nm using a constant center-to-center turn distance of 1478 nm. Given a constant outer diameter (75 μm edge-to-edge, 80 μm corner-to-corner), turn width (1.0 μm edge-to-edge, 1.1 μm corner-to-corner), and turn spacing (0.46 μm edge-to-edge, 0.50 μm corner-to-corner), the number of

turns was varied and represented as the percentage of the total diameter left open at its core. The open core percentage was tested at 10.9% (23 turns), 22.6% (20 turns), 34.4% (17 turns), 46.2% (14 turns), 57.9% (11 turns), and 65.8% (9 turns). All device geometries were tested using representative current input of 1 nA through the interface pad at the center of the inductor. The optimized device geometry was used to model the magnetic response when coupled with the model neuron. The effects of various substrates were tested using the same input current by varying the material properties of a $25 \times 50 \times 100 \mu\text{m}$ block beneath the device between glass, $\varepsilon = 4.7$, $\mu = 1$, $\sigma = 2.3 \times 10^{-21} \text{ S m}^{-1}$; polyimide, $\varepsilon = 3.8$ [36], $\mu = 1$, $\sigma = 6.7 \times 10^{-18} \text{ S m}^{-1}$; parylene, $\varepsilon = 3.1$ [36], $\mu = 1$, $\sigma = 1.136 \times 10^{-15} \text{ S m}^{-1}$; and silicon of various conductivities, $\varepsilon = 11.68$, $\mu = 1$, $\sigma = (0.01, 0.1, 1, 10, 100, 1000, 10000, 100000) \text{ S m}^{-1}$ (0.001 $\Omega \text{ cm}$ to 10000 $\Omega \text{ cm}$). Magnetic field values were extracted from the model either linearly across a $120 \mu\text{m} \times 1 \mu\text{m} \times 1 \mu\text{m}$ region of interest (ROI) centered at various Y coordinates on the $Z = 0$ plane, or volumetrically within a $40 \mu\text{m} \times 40 \mu\text{m} \times 10 \mu\text{m}$ ROI centered at the cell-device interface pad, in the X , Y , and Z axes. For linear scans, the mean and standard deviation of the absolute magnetic field magnitude were taken along the Y/Z axes within the ROI. Separately, absolute magnetic field amplitude was taken along a 20 μm , Y -aligned line on the $Z = 0$ plane, centered on the neurite 2 μm away from the input port (supplementary figure 1) to compare the magnetic field amplitude of the neuron with and without the presence of the device. Volumetric values averaged the Z component of the magnetic field across the ROI. For optimizations of device geometry and substrate testing, the Z component of the magnetic field output was extracted at an XZ slice of the model arena at the Y coordinate corresponding to the center of the coil and used to compare the output of each model instance.

3. Results

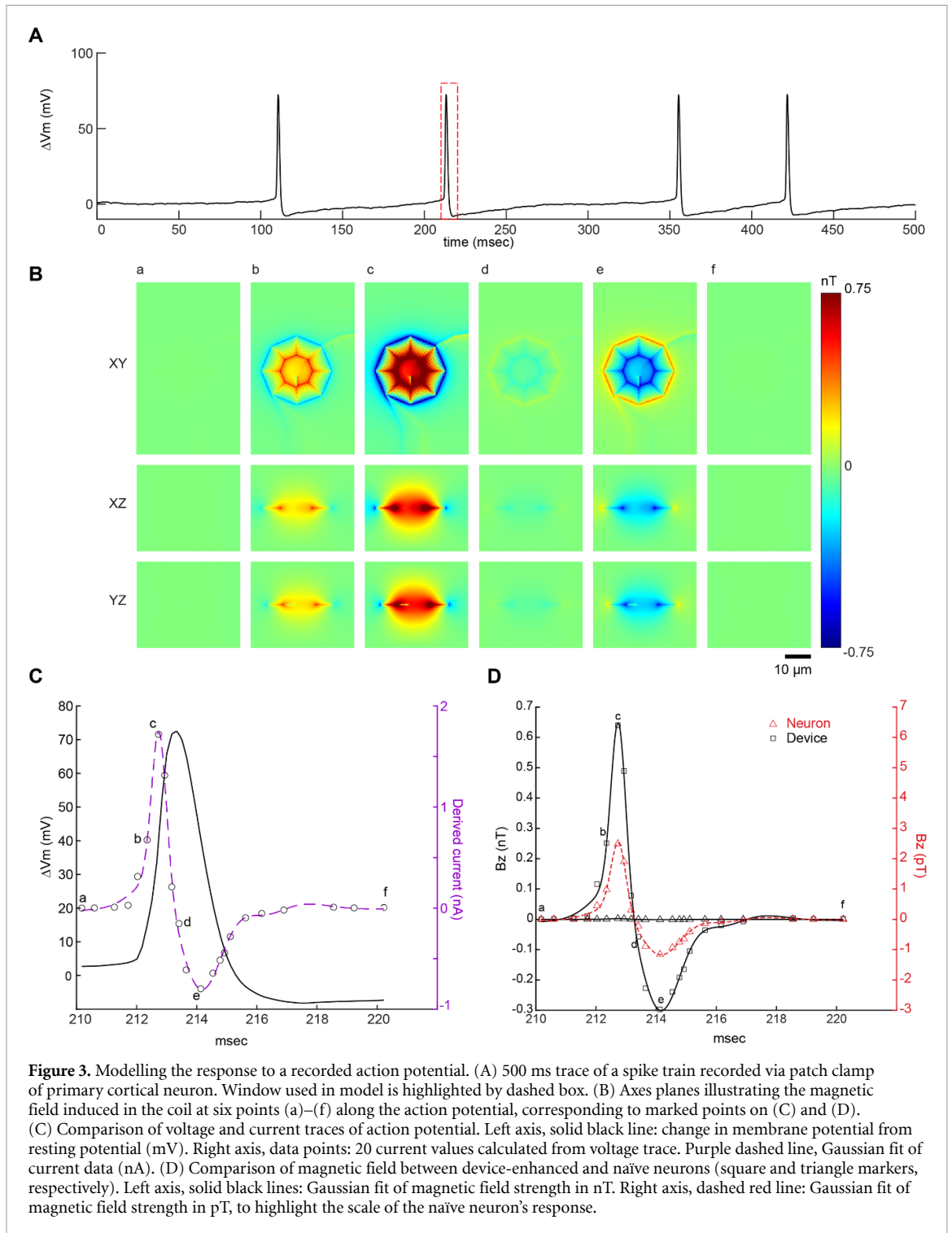
3.1. Enhancement of intrinsic NMFs by nanofabricated coils

In order to explore the feasibility of enhancing intrinsic NMFs by nanofabricated coils (nanocoils) interfaced with single neurons, we generated a realistic finite element model of a cell coupled to device and quantified the magnetic field response to current injected into the cell (figure 1). The model uses morphology extracted from primary cortical neurons injected with fluorescently labeled biocytin via patch micropipette electrodes (figure 1(A) and supplementary figure 2). Neurons grew on glass coverslips or nanofabricated devices for up to 24 DIV (figure 1(B)). We input a series of key current values into the model, extracted and calculated from a patch clamp recording of cells on coverslips (figure 3(c)),



with a peak of 1.7 nA intracellular current in the model cell (figure 1(C)), resulting in intracellular electric fields of up to $1.2 \text{ mV } \mu\text{m}^{-1}$ and extracellular electric fields up to $30 \text{ } \mu\text{V } \text{mm}^{-1}$ within $2 \text{ } \mu\text{m}$ of the neurite membrane (supplementary figure 2(C)), and the transmembrane electric field gradient reaching $11 \text{ mV } \text{nm}^{-1}$ as previously seen both *in vitro* and *in vivo* [37]. The absolute amplitude of the magnetic field observed near the neuron in response to current injection reached values of up to 0.51 nT and decays to <1% of peak signal within an average of $30 \text{ } \mu\text{m}$ of the neuron, similarly to previous models of single-cell NMFs [11, 12]. We next quantified the magnetic field amplitude at a volume surrounding the same 1.7 nA current-injected neuron coupled to a nanocoil (figure 1(D)). The neuronal membrane was coupled to the interface pad in the middle of the nanocoil (figure 1(D), a). The magnetic field amplitude at various line scans across the X axis (figure 1(D), (a–e)) reached values of up to 1.6 nT and decayed to <1% of peak within an average of $19 \text{ } \mu\text{m}$ from the outer turns of the nanocoil. In the case of line a (figure 1(D)), which crosses the interface pad, the magnetic field decayed to <1% of peak an average

of $46 \text{ } \mu\text{m}$ from the interface pad. We quantified the spatial distribution of NMFs in the naïve neuron not coupled to the device within a $1 \text{ } \mu\text{m}$ by $1 \text{ } \mu\text{m}$ cross sectional area around various line scans across the X axis and found that across three representative somatic and neurite compartments (figures 1(c), (a–c) and (E)) the full widths at half maximum (FWHM) of magnetic field magnitude were (a) $2.7 \text{ } \mu\text{m}$, (b, soma) $7.9 \text{ } \mu\text{m}$, and (c) $7.1 \text{ } \mu\text{m}$. In contrast, the spatial distribution of magnetic fields near a neuron coupled to a device across five representative regions (figures 1(D), (a–e) and (F)) was spatially enhanced with FWHM of (a) $67 \text{ } \mu\text{m}$, (b) $72 \text{ } \mu\text{m}$, (c) $62 \text{ } \mu\text{m}$, (d) $46 \text{ } \mu\text{m}$, and (e, ground pad) $16 \text{ } \mu\text{m}$. The magnetic field amplitude of the neuron itself was not significantly changed when coupled to the device, reaching levels of up to 0.60 nT in the neurite of the naïve neuron and 0.25 nT in the neurite of the neuron enhanced by the device, measured $2 \text{ } \mu\text{m}$ from the neurite input port (supplementary figure 1), within the bounds of minimal magnetic interference. In summary, the magnetic field amplitude output by the device driven by cellular potentials is more than three times greater at its peak (1.6 nT vs 0.51 nT) across a ten times wider



lateral distance ($72 \mu\text{m}$ from the device vs $7.1 \mu\text{m}$ from the neurite) than the intrinsic NMF. Looking at a $40 \times 40 \times 10 \mu\text{m}$ voxel, discussed below, this results in a 250-fold spatial enhancement (640 pT vs 2.5 pT , see figure 3).

3.2. Analysis of device geometry

Based on the initial geometry used to quantify the magnetic response of a neuron-device interface, we performed optimizations of design features to explore maximal transduction while obeying

nanofabrication limitations (figure 2). Three main parameters tested included the vertical thickness of the device metallization layer (figures 2(A)–(C)), the lateral width of the nanocoil turns (figures 2(D)–(F)), and the number of turns as represented by the open core percentage (figures 2(G)–(I)). For each parameter value, we compared the mean z -axis component of the magnetic flux density (B_z) within a ROI across a XZ slice over the center of the device, spanning $50 \mu\text{m}$ along the x axis, and $12.5 \mu\text{m}$ along the z axis. The bottom of the slice was aligned

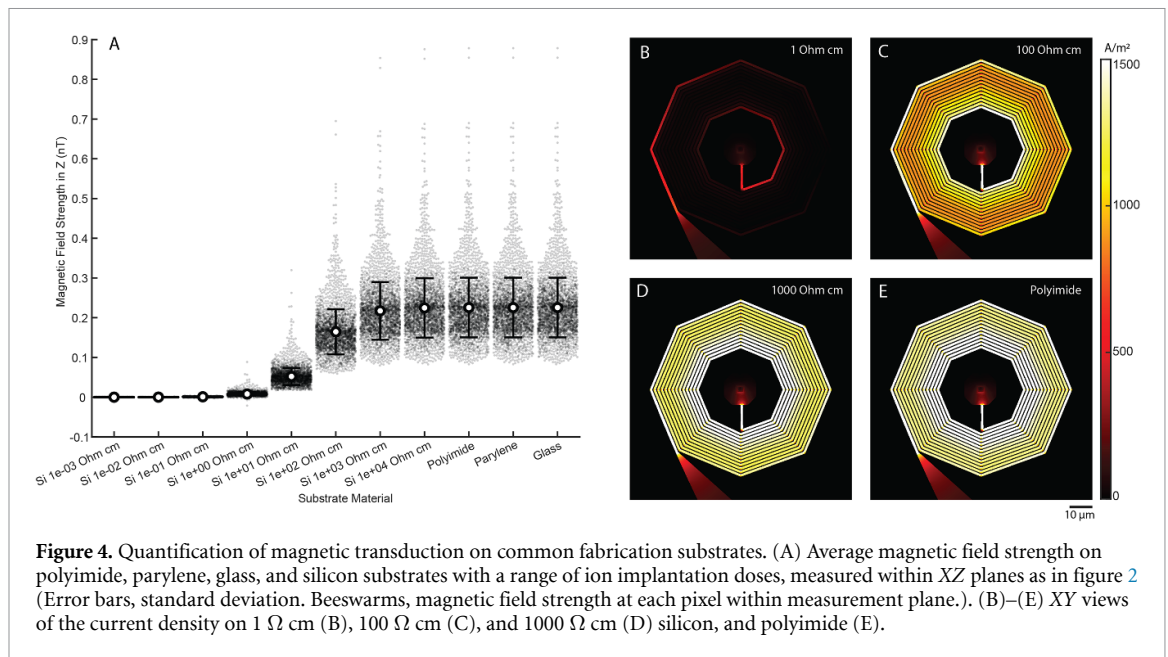


Figure 4. Quantification of magnetic transduction on common fabrication substrates. (A) Average magnetic field strength on polyimide, parylene, glass, and silicon substrates with a range of ion implantation doses, measured within XZ planes as in figure 2 (Error bars, standard deviation. Beeswarms, magnetic field strength at each pixel within measurement plane.). (B)–(E) XY views of the current density on 1 Ω cm (B), 100 Ω cm (C), and 1000 Ω cm (D) silicon, and polyimide (E).

to $z = 0$, coplanar with the bottom plane of the device (figures 2(A), (B), (D), (E), (G) and (H), bottom panel).

We used the initial geometry (turn width of 334 nm, core 57.9%) and varied the vertical gold layer thickness by extruding the device to values of 100, 500, 1000, and 1500 nm (figures 2(A)–(C)), yielding average field strength $B_z = 0.030 \pm 0.013$ nT, 0.086 ± 0.033 nT, 0.12 ± 0.04 nT, and 0.13 ± 0.05 nT, respectively. Proceeding with a 500 nm thick gold layer, we next quantified the effect of nanocoil turn width on the average magnetic field strength B_z at the device surface (figures 2(D)–(F)). Turn width was set to 540, 730, 940, and 1020 nm, yielding average field strength $B_z = 0.11 \pm 0.04$, 0.13 ± 0.04 , 0.14 ± 0.04 and 0.14 ± 0.05 nT, respectively (figure 2(F)). Predictably, the widest path induced the strongest magnetic field strength. We turned to testing the effect of the total number of turns, while maintaining a constant outer diameter (80 μm), neural interface pad diameter (when allowed by the core size, 14 μm), coil thickness (500 nm), turn width (1020 nm), and turn spacing (1478 nm) (figures 2(G)–(I)). We represent this as the ratio of the inner to the outer diameter, or the percentage of the outer diameter that makes up the open core of the nanocoil. We tested values 10.9% (23 turns), 22.6% (20 turns), 34.4% (17 turns), 46.2% (14 turns), 57.9% (11 turns), and 65.8% (9 turns), which yielded mean $B_z = 0.27 \pm 0.16$, 0.25 ± 0.12 , 0.22 ± 0.08 , 0.18 ± 0.06 , 0.14 ± 0.04 and 0.11 ± 0.03 nT, respectively (figure 2(I)). Predictably, smaller cores produced higher peak magnetic field strength perpendicular to the plane of the coil (peak $B_z = 1.1$, 0.85, 0.79, 0.73, 0.67 and 0.52) while the minimum field strength observed at the periphery of the ROI remained stable across different conditions (min $B_z = 0.057$, 0.058, 0.061, 0.064, 0.060, and 0.061 nT).

3.3. Single neuron activity on optimized device

We analyzed the magnetic field developing at the neuron-device interface during a typical AP selected from a series of spontaneously occurring spikes recorded via patch clamp (figure 3(a)). Modeled magnetic field was averaged across a $40 \times 40 \times 10$ μm voxel extending 20 μm to each side of the center of the coil, and 5 μm above and below the coil (figure 3(B)). The same voxel dimensions were used to average the modeled magnetic output of the naïve neuron. Absolute AP amplitude was 72 mV, and the after-hyperpolarization voltage was -8.2 mV (figure 3(c)). The AP voltage trace was run through the equivalent circuit of a neuron to derive the current trace (figure 3(c), purple). The current peaked at 1.7 nA during depolarization and had a minimum of -0.80 nA during the after-hyperpolarization stage. The magnetic field perpendicular to the plane of the neuron and nanocoil peaked at 2.5 pT for the naïve neuron, and at 640 pT for the neuron enhanced by the device. The magnetic field perpendicular to the plane of the geometry induced by the down-swung current was -1.2 pT for the naïve neuron and -300 pT for the enhanced neuron. The overall spatial enhancement of the transduced magnetic field output within a voxel was 250-fold higher than the intrinsic NMF.

3.4. Substrate testing

To evaluate performance on substrates compatible with nanolithography that are commonly used for implantable devices, we quantified the magnetic transduction of nanocoils embedded on dielectric substrates including glass, parylene and polyimide, and on silicon with various levels of doping (figure 4). High resistivity silicon (1000 Ω cm and 10 000 Ω cm) and all dielectric substrates displayed strong induced magnetic fields (figure 4(A)) with average magnetic

field strength of 0.23 ± 0.08 nT for dielectrics, 0.22 ± 0.07 nT for $10\,000\ \Omega\ \text{cm}$ Si, and 0.22 ± 0.07 nT for $1000\ \Omega\ \text{cm}$ Si. Low resistivity silicon (0.001, 0.01, and $0.1\ \Omega\ \text{cm}$) demonstrated predictable current shunting, and weak induced magnetic fields, with average field strength of $4.8 \times 10^{-6} \pm 3.8 \times 10^{-4}$ nT, $8.5 \times 10^{-5} \pm 2.1 \times 10^{-4}$ nT, and $9.7 \times 10^{-4} \pm 7.1 \times 10^{-4}$ nT, respectively). Silicon substrates with resistivities of 1, 10, and 100 showed an intermediate effect, with average field strength of 0.0080 ± 0.0048 , 0.052 ± 0.022 , and 0.16 ± 0.06 nT, respectively). Current density was largely in proportion to field strength, reaching maximal levels of $880\ \text{A}\ \text{m}^{-2}$, $2400\ \text{A}\ \text{m}^{-2}$, $2800\ \text{A}\ \text{m}^{-2}$, and $2800\ \text{A}\ \text{m}^{-2}$ for 1, 100, $1000\ \Omega\ \text{cm}$ Silicon and for Polyimide, respectively (figures 4(B)–(E)).

4. Discussion

Our model validates a new principle for amplifying neurogenic magnetic fields by interfacing single neurons with nanofabricated flat spiral coils. The junction formed between cell and device relies on tight electrical coupling at the interface pad and generates magnetic fields that are enhanced both spatially and in amplitude, compared with the driving NMF. We show that the predicted magnetic field magnitude in response to neural currents surrounding the device is more than three-fold higher in peak amplitude compared to intrinsic NMF, reaching 1.6 nT in the plane of the coil. Averaging the signal over a volume of $40 \times 40 \times 10\ \mu\text{m}^3$ results in 640 pT compared with 2.5 pT for a naïve neuron and an overall spatial enhancement of the transduced magnetic field output of more than 250-fold. Our approach brings about immediate relevance to *in vitro* magnetometry but also has potential relevance to modalities such as MRI and MEG, whereby arrays of nanofabricated devices of sufficient density can modulate signal change in response to neuronal activation. Our approach could provide a way to overcome the theoretical limitations of spatial resolution and sensitivity of these modalities that thus far precluded detecting micrometer scale picoTesla events without transcranial wiring at the time of recording.

Effective coupling for remote electromagnetic detection depends on nanofabrication features that dictate impedance and inductance [38–40]. The geometric optimization delivered by our model provides recipes that can be applied on unique substrates for increased magnetic transduction, while adhering to the practical limitations of nanofabrication techniques. One unique avenue for application is nanofabrication of nanocoils on emerging nitrogen vacancy (NV) diamond substrates used for fluorescence-based micro-magnetometry [41, 42]. This technology enables highly sensitive magnetic detection of resolved 400 pT transient magnetic events resulting from APs in nerve preparations

[43] and single-cell superparamagnetic nanoparticle internalization *in vitro* [44]. These studies could benefit from enhanced fields by arrays of nanocoils that can provide multiplexed single-neuron readouts of neuronal networks, and this modality is sensitive enough to capture the theoretical magnetic output of a single nanocoil device. More broadly, NV diamond magnetometry employs microwave resonance at the 2.87 GHz regime, inviting integration of capacitors into the nanocoil device for microwave resonance and high spatial resolution modulation of fluorescence by magnetic fields. Lithography of high aspect-ratio inductors offers reduced impedance and increased inductive coupling but can also present constraints due to possible structural collapse of device features [45–47]. In this study, we analyzed metallization layers ranging between 100 nm and $1.5\ \mu\text{m}$, and show a predictably high magnetic field of 0.13 nT produced at the highest thickness with a 1 nA current. We find that thickness of 500 nm with 1020 nm turn width, yielded a comparably strong magnetic field of 0.14 nT, with features that maintain 1:1 or smaller aspect ratio and are well within the capabilities of electron beam lithography and Au growth techniques. Other significant features include the interface pad at the core of the device that acts as a common electrode driving the magnetic field generation at the nanocoil. The size of the coil's open core impacts the size of the interface pad, turn density and overall magnetic field strength. A core with a diameter only 10.9% the diameter of the nanocoil was found to produce the highest peak magnetic field, (0.27 ± 0.16 nT) but with very high standard deviation across the $12.5 \times 50\ \mu\text{m}$ plane tested. A core of a 46.2%, allowed for a sufficiently large $14.4\ \mu\text{m}$ interface pad, a low variability magnetic field of 0.18 ± 0.06 nT and overall optimal performance.

Our model mimics the generation of ionic currents during APs at sub-cellular neurite morphologies on a flat device *in vitro*. Currents propagating in neuronal compartments induce magnetic fields that rotate around the axis of neurite at specific orientations during synaptic events and aggregate to form a typical MEG signal measured outside of the brain [7, 9]. A flat spiral nanocoil interfaced with a neuron is predicted to generate magnetic fields rotating about the turns of the coil, aggregating to a large field spread over an area perpendicular to the plane of the substrate irrespective of the original NMF alignment to the detector. This offers a new repertoire of MEG measurements from untapped anatomical orientations and depths *in vivo*, assuming sufficiently dense multiple aligned coil arrays are implanted. We examined magnetic fields on commonly used implantable substrates including high resistivity silicon, glass, polyimide and parylene. We find no magnetic field loss on these substrates, leading to potential long-term implantation of nanocoils leveraging known chronic biocompatibility for

these substrates. Flexible substrates are of particular importance and can facilitate MEG signal enhancements when implanted similarly to dense electrocardiogram devices that conform to anatomical features in the brain [48, 49]. Such an array would theoretically allow for measurement of single cell activity *in vivo* without the need for transcranial wiring. Moreover, previous MRI phantom measurements of a 30 μm wire demonstrate detectability of fields as low as 200 pT for a $2.5 \times 2.5 \times 6$ mm voxel [50]. Given that our 80 μm device produces a 640 pT volumetric magnetic field, it is feasible that the field produced by a single device coupled with a firing neuron will be detectable via MRI. In conclusion, our quantifications institute a foundation for synthesizing minimally invasive electromagnetic sensors for detecting brain activity and can serve as a broad protocol for quantifying sensitivity at the single cell level.

Data availability statement

The data that support the findings of this study are available upon reasonable request from the authors.

Author contributions

A H, M G and J K P designed the research. J K P and M G performed the research. J K P, M G and Y G analyzed the data. A A, M D and A H fabricated the device, J K P performed cell imaging and patch clamp experiments. J K P and A H wrote the manuscript.

Conflict of interest

The authors declare no competing interests.

Funding

This work was supported by the National Institute of Neurological Disorders and Stroke and the Office of the Director's Common Fund at the National Institutes of Health (Grant DP2NS122605 to A H), the National Institute of Biomedical Imaging and Bioengineering (Grant K01EB027184 to A H) and the Wisconsin Alumni Research Foundation (WARF).

ORCID iDs

Jack Phillips  <https://orcid.org/0000-0002-5362-8833>

Alireza Ashtiani  <https://orcid.org/0000-0001-9272-1929>

Aviad Hai  <https://orcid.org/0000-0002-4556-3048>

References

- [1] Lebedev M A and Nicolelis M A L 2006 Brain-machine interfaces: past, present and future *Trends Neurosci.* **29** 536–46
- [2] Homer M L, Nurmikko A V, Donoghue J P and Hochberg L R 2013 Sensors and decoding for intracortical brain computer interfaces *Annu. Rev. Biomed. Eng.* **15** 383–405
- [3] Chandrasekaran S et al 2021 Historical perspectives, challenges, and future directions of implantable brain-computer interfaces for sensorimotor applications *Bioelectron. Med.* **7** 14
- [4] Spira M E and Hai A 2013 Multi-electrode array technologies for neuroscience and cardiology *Nat. Nanotechnol.* **8** 83–94
- [5] Frank J A, Antonini M-J and Anikeeva P 2019 Next-generation interfaces for studying neural function *Nat. Biotechnol.* **37** 1013–23
- [6] Buzsáki G, Anastassiou C A and Koch C 2012 The origin of extracellular fields and currents—EEG, ECoG, LFP and spikes *Nat. Rev. Neurosci.* **13** 407–20
- [7] Baillet S 2017 Magnetoencephalography for brain electrophysiology and imaging *Nat. Neurosci.* **20** 327–39
- [8] Müller-Putz G R 2020 Electroencephalography *Handbook of Clinical Neurology Brain-Computer Interfaces* vol 168, ed N F Ramsey and J D R Millán (Amsterdam: Elsevier) ch 18, pp 249–62
- [9] Boto E et al 2017 A new generation of magnetoencephalography: room temperature measurements using optically-pumped magnetometers *NeuroImage* **149** 404–14
- [10] Roth B J and Wikswo J P 1985 The magnetic field of a single axon. A comparison of theory and experiment *Biophys. J.* **48** 93–109
- [11] Xue Y, Gao J-H and Xiong J 2006 Direct MRI detection of neuronal magnetic fields in the brain: theoretical modeling *NeuroImage* **31** 550–9
- [12] Blagoev K B et al 2007 Modelling the magnetic signature of neuronal tissue *NeuroImage* **37** 137–48
- [13] Isakovic J, Dobbs-Dixon I, Chaudhury D and Mitrecic D 2018 Modeling of inhomogeneous electromagnetic fields in the nervous system: a novel paradigm in understanding cell interactions, disease etiology and therapy *Sci. Rep.* **8** 12909
- [14] Vrba J and Robinson S E 2001 Signal processing in magnetoencephalography *Methods* **25** 249–71
- [15] Bandettini P A, Petridou N and Bodurka J 2005 Direct detection of neuronal activity with MRI: fantasy, possibility, or reality? *Appl. Magn. Reson.* **29** 65–88
- [16] Petridou N, Plenz D, Silva A C, Loew M, Bodurka J and Bandettini P A 2006 Direct magnetic resonance detection of neuronal electrical activity *Proc. Natl Acad. Sci.* **103** 16015–20
- [17] Sundaram P, Nummenmaa A, Wells W, Orbach D, Orringer D, Mulkern R and Okada Y 2016 Direct neural current imaging in an intact cerebellum with magnetic resonance imaging *Neuroimage* **132** 477–90
- [18] Sadleir R J, Fu F, Falgas C, Holland S, Boggess M, Grant S C and Woo E J 2017 Direct detection of neural activity *in vitro* using magnetic resonance electrical impedance tomography (MREIT) *Neuroimage* **161** 104–19
- [19] Sajib S Z K, Chauhan M, Kwon O I and Sadleir R J 2021 Magnetic-resonance-based measurement of electromagnetic fields and conductivity *in vivo* using single current administration—a machine learning approach *PLoS One* **16** e0254690
- [20] Beisteiner R, Gomiscek G, Erdler M, Teichtmeister C, Moser E and Deecke L 1995 Comparing localization of conventional functional magnetic resonance imaging and magnetoencephalography *Eur. J. Neurosci.* **7** 1121–4
- [21] Mackert B-M, Leistner S, Sander T, Liebert A, Wabnitz H, Burghoff M, Trahms L, Macdonald R and Curio G 2008 Dynamics of cortical neurovascular coupling analyzed by simultaneous DC-magnetoencephalography and time-resolved near-infrared spectroscopy *Neuroimage* **39** 979–86
- [22] Logothetis N K 2008 What we can do and what we cannot do with fMRI *Nature* **453** 869–78
- [23] Li W, Parigi G, Fragai M, Luchinat C and Meade T J 2002 Mechanistic studies of a calcium-dependent MRI contrast agent *Inorg. Chem.* **41** 4018–24
- [24] Okada S, Bartelle B B, Li N, Breton-Provencher V, Lee J J, Rodriguez E, Melican J, Sur M and Jasanoff A 2018

- Calcium-dependent molecular fMRI using a magnetic nanosensor *Nat. Nanotechnol.* **13** 473–7
- [25] Barandov A, Bartelle B B, Williamson C G, Loucks E S, Lippard S J and Jasanoff A 2019 Sensing intracellular calcium ions using a manganese-based MRI contrast agent *Nat. Commun.* **10** 897
- [26] Lee T, Cai L X, Lelyveld V S, Hai A and Jasanoff A 2014 Molecular-level functional magnetic resonance imaging of dopaminergic signaling *Science* **344** 533–5
- [27] Hai A and Jasanoff A 2015 Molecular fMRI *Brain Mapping* ed A W Toga (Waltham, MA: Academic) pp 123–9
- [28] Hai A, Cai L X, Lee T, Lelyveld V S and Jasanoff A 2016 Molecular fMRI of serotonin transport *Neuron* **92** 754–65
- [29] Li N and Jasanoff A 2020 Local and global consequences of reward-evoked striatal dopamine release *Nature* **580** 239–44
- [30] Hai A, Dormann A, Shappir J, Yitzchaik S, Bartic C, Borghs G, Langedijk J P M and Spira M E 2009 Spine-shaped gold protrusions improve the adherence and electrical coupling of neurons with the surface of micro-electronic devices *J. R. Soc. Interface* **6** 1153–65
- [31] Hai A, Kamber D, Malkinson G, Erez H, Mazurski N, Shappir J and Spira M E 2009 Changing gears from chemical adhesion of cells to flat substrata toward engulfment of micro-protrusions by active mechanisms *J. Neural Eng.* **6** 066009
- [32] Hai A, Shappir J and Spira M E 2010 In-cell recordings by extracellular microelectrodes *Nat. Methods* **7** 200–2
- [33] Hai A, Shappir J and Spira M E 2010 Long-term, multisite, parallel, in-cell recording and stimulation by an array of extracellular microelectrodes *J. Neurophysiol.* **104** 559–68
- [34] Spira M E and Hai A 2013 Multi-electrode array technologies for neuroscience and cardiology *Nature Nanotechnol.* **8** 83–94
- [35] Bricault S, Barandov A, Harvey P, DeTienne E, Hai A and Jasanoff A 2020 Image-guided neural activity manipulation with a paramagnetic drug *Nat. Commun.* **11** 136
- [36] Iba S, Sekitani T, Kato Y, Someya T, Kawaguchi H, Takamiya M, Sakurai T and Takagi S 2005 Control of threshold voltage of organic field-effect transistors with double-gate structures *Appl. Phys. Lett.* **87** 023509
- [37] Anastassiou C A, Perin R, Markram H and Koch C 2011 Ephaptic coupling of cortical neurons *Nat. Neurosci.* **14** 217–23
- [38] Hai A, Spanoudaki V C, Bartelle B B and Jasanoff A 2019 Wireless resonant circuits for the minimally invasive sensing of biophysical processes in magnetic resonance imaging *Nat. Biomed. Eng.* **3** 69–78
- [39] Qian W and Qian C 2019 Frequency modulated parametric oscillation for antenna powered wireless transmission of voltage sensing signals *IEEE Trans. Biomed. Circuits Syst.* **13** 1783–91
- [40] Jasanoff A P, Spanoudaki V and Hai A 2020 Tunable detectors *US Patent* 20200046224A1
- [41] Maze J R et al 2008 Nanoscale magnetic sensing with an individual electronic spin in diamond *Nature* **455** 644–7
- [42] Arai K, Belthangady C, Zhang H, Bar-Gill N, DeVience S J, Cappellaro P, Yacoby A and Walsworth R L 2015 Fourier magnetic imaging with nanoscale resolution and compressed sensing speed-up using electronic spins in diamond *Nat. Nanotechnol.* **10** 859–64
- [43] Barry J F, Turner M J, Schloss J M, Glenn D R, Song Y, Lukin M D, Park H and Walsworth R L 2016 Optical magnetic detection of single-neuron action potentials using quantum defects in diamond *Proc. Natl Acad. Sci.* **113** 14133–8
- [44] Davis H C, Ramesh P, Bhatnagar A, Lee-Gosselin A, Barry J F, Glenn D R, Walsworth R L and Shapiro M G 2018 Mapping the microscale origins of magnetic resonance image contrast with subcellular diamond magnetometry *Nat. Commun.* **9** 131
- [45] Vieu C, Carcenac F, Pépin A, Chen Y, Mejias M, Lebib A, Manin-Ferlazzo L, Couraud L and Launois H 2000 Electron beam lithography: resolution limits and applications *Appl. Surf. Sci.* **164** 111–7
- [46] Noga D E, Lawson R A, Lee C-T, Tolbert L M and Henderson C L 2009 Understanding pattern collapse in high-resolution lithography: impact of feature width on critical stress *Proc. SPIE* **7273** 727334
- [47] Lee H, Sun E, Ham D and Weissleder R 2008 Chip-NMR biosensor for detection and molecular analysis of cells *Nat. Med.* **14** 869–74
- [48] Viventi J et al 2011 Flexible, foldable, actively multiplexed, high-density electrode array for mapping brain activity *in vivo* *Nat. Neurosci.* **14** 1599–605
- [49] Park D-W et al 2014 Graphene-based carbon-layered electrode array technology for neural imaging and optogenetic applications *Nat. Commun.* **5** 5258
- [50] Bodurka J and Bandettini P A 2002 Toward direct mapping of neuronal activity: MRI detection of ultraweak, transient magnetic field changes *Magn. Reson. Med.* **47** 1052–8